

¹ **Space-Time Ambiguity Function for** ² **Electronically Scanned ISR**

John Swoboda,¹ Joshua Semeter,¹ Philip Erickson²

Corresponding author: J. P. Swoboda, Department of Electrical & Computer Engineering,
Boston University, 8 Saint Marys Street Boston, MA 02215, USA. (swoboj@bu.edu)

¹Department of Electrical & Computer
Engineering, Boston University, Boston,
Massachusetts, USA.

²Atmospheric Science Division, MIT
Haystack Observatory, Westford
Massachusetts, USA.

Electronically steerable array (ESA) technology has recently been used in incoherent scatter radars (ISR). These arrays allow for pulse-to-pulse steering of the antenna beam to collect data in a three dimensional region. This is in direct contrast to dish based antennas where acquisition is limited to take data in a two dimensional slice. This new paradigm allows for more flexibility in the measurement of ionospheric plasma parameters.

Currently these systems are operating in the high latitude region where the ionosphere is highly dynamic in both space and time. Because of the highly dynamic nature of the ionosphere in this region it is important to differentiate between artifacts and the true behavior of the plasma. Often the three dimensional data is fitted in a spherical coordinate space and then the parameters are interpolated to a Cartesian grid. This and other sources of error could be impacting the reconstructions of the plasma parameters.

To take advantage of the new flexibility of ESA system we present a new way of analyzing ISR through use of the space-time ambiguity function. This concept is similar to the range ambiguity function that is used in traditional ISR for scanning antenna systems but has been extended to all spatial dimensions along with time as well.

The use of this new ambiguity function allow us to pose this problem in terms of a linear inverse problem for the lags of the intrinsic plasma autocorrelation function. From this we can explore the impact of non-uniformity in the plasma parameters in both time and space. Along with showing pos-

25 sible artifacts we will begin to discuss ways of reducing them and improv-
26 ing the quality of data products from electronically steerable ISRs.

1. Introduction

Incoherent scatter radar (ISR) is a powerful tool for exploring the ionosphere. These systems can give measurements of electron density N_e , ion temperature T_i , electron temperature T_e , ion velocity V_i and other plasma parameters [Dougherty and Farley, 1960; Farley et al., 1961; Dougherty and Farley, 1963; Hagfors, 1961]. These parameters are measured by fitting a nonlinear theoretic autocorrelation function (ACF) model derived from first principles physics to an estimated time autocorrelation or, alternatively, the power spectrum of the radar signal scattered off of random electron density fluctuations [Lehtinen and Huuskonen, 1996].

This is an estimation of a second order statistic of an inherently random process from the scattering of electrons. In order to get an estimate of the ACF with reasonable statistical properties numerous pulses have to be averaged together. With traditional dish antennas the ISR system would build these statistics in a limited number of ways. One method consists of pointing the radar beam in a specific direction and hold it there until enough pulses were integrated to get the desired statistics. Alternatively, the beam could be scanned through a field of view and collect pulses while moving. These techniques have an implicit assumption about the uniformity of the plasma parameters within a volume defined by pulse shape and beam while pulses are being integrated. This leads to the assumption of the stationarity of the ACF within a temporal and spatial resolution cell of the radar.

In many cases, especially in the high latitude ionosphere, this stationarity assumption is not met. Phenomena such as polar cap patches that may be drifting at

greater than 1km/s, and thus the residency time of a particular plasma parcel within a radar beam may be much shorter than the integration time required to estimate an ACF[Dahlgren *et al.*, 2012a]. In the auroral zone, ionospheric variations produced by auroral particle precipitation on similarly short time scales compared to the integration period [Zettergren *et al.*, 2008].

Recently electronically steerable array (ESA) technology has started to be leveraged by the ISR community. The Advance Modular Incoherent Scatter Radar (AMISR) systems have already been deployed both at the Poker Flat Alaska (PFISR) and Resolute Bay Canada (RISR). The EISCAT-3D project is currently being developed using phased array technology as well and will be capable of multistatic processing. These new systems are already being used in a number of different ways including creating volumetric reconstructions of plasma parameters [Semeter *et al.*, 2009; Nicolls and Heinselman, 2007; Dahlgren *et al.*, 2012a, b]. These reconstructions mainly consist of taking ISR data after parameters have been fit in a spherical coordinate system and then interpolate them into a Cartesian space.

These new ESA based systems differentiate themselves from dish antennas in a fundamental way. Instead of dwelling in a single beam or scanning along a prescribed direction, an ESA can move to a different beam position within its field of view on a pulse by pulse basis. This yields a new flexibility to integrate different beams in such a way that the original velocity of the plasma can be unknown. This can help to relax the assumption of stationarity in that now the plasma can move into a different beam and have the returns from the same plasma be integrated together. As opposed

to the case with a dish antenna where the returns from different plasma would be improperly averaged together.

In order to take advantage of this new flexibility this work puts forth the idea of the space-time ambiguity function. This concept extends the range ambiguity to all three spatial dimensions along with time. The goal of this paper is to develop the formalism for treating space-time ambiguity for electronically steerable ISRs or ISRs that are capable of sampling a given volume on a pulse-by-pulse basis. The impact of the three-dimensional ambiguity on moving plasma will be shown through specific cases related to the polar cap patches. A simulation of a polar cap patch using a full ISR simulator, which creates ISR data at the I/Q level, will be shown. Lastly we will explore a number of different ways that could improve measurements from electronically steerable ISR systems.

2. Space-Time Ambiguity

The space-time ambiguity can be thought of as a kernel to a combined volume and time integration operator. In the end this ambiguity can be represented as kernel in a Fredholm integral equation,

$$\rho(\mathbf{r}_s) = \int K(\mathbf{r}_s, \mathbf{r}) R(\mathbf{r}) d\mathbf{r} \quad (1)$$

where, for ISR, $R(\mathbf{r})$ is the lag of the autocorrelation function at a specific time and position.

By using this formulation many parallels between ISR and classic camera blurring problems can be made. In cameras blurring can take place when an object moves over a space covered by one pixel while the shutter is open and the CCD is collecting photons. A diagram of this can be seen in Figure 1. The same holds for ISR except that the pixels are no longer square and instead are determined by the beam shape and pulse pattern. This is shown in the diagrams in Figure 2.

Before we derive this ambiguity function we will start with defining our coordinate system.

2.1. Coordinate System Definitions

Our three dimensional coordinate system is defined as $\mathbf{r} = [x, y, z]^T$. For this coordinate system, $\mathbf{r} = [0, 0, 0]^T$ at the location of the radar and thus $r = |\mathbf{r}|$, also known as the range variable. This allows for the use of polar coordinates $\mathbf{r} = [r, \theta, \phi]^T$ where θ is the physical elevation angle, ϕ is the physical azimuth angle.

The radar will sample this space into a set of discrete points which will be referred to as $\mathbf{r}_s = [x_s, y_s, z_s]^T$ along with the discretized range $r_s = |\mathbf{r}_s|$. The sampled space will consist of a number of points which are the combinations of range gates and number of beams. These points can also be referred in the polar coordinates $\mathbf{r}_s = [r_s, \theta_s, \phi_s]^T$, where θ_s is the sampled elevation angle, ϕ_s is the sampled azimuth angle.

For notation purposes we use two different sets of time commonly known in radar literature as fast-time, n and slow-time, t [Richards, 2005]. Fast-time is used to describe processes with correlation time less than one pulse repetition interval (PRI).

Slow-time will be used for processes that decorrelate in time on the order of the system's PRI. In order to form estimates of the ACFs, with desired statistical properties, it is assumed that the plasma parameters will change on the order of many tens to hundreds of PRIs in their stationary reference frame. Generally for incoherent scatter in the E-region of the ionosphere and above the decorrelation time is less than a PRI, thus the ACFs are formed over fast-time.

The terms n and t will represent continuous variables while n_s and t_s will be the fast time and slow time parameters sampled by the radar. The sampling rate of n_s will be that of the A/D converters. The sampling of t_s can at the highest rate, be the PRI. At its lowest, it can be sampled once in a non-coherent processing interval (NCPI), or a period of time it takes the radar to average the desired number of pulses.

2.2. Derivation

The basic physical mechanism behind ISR is that electron density fluctuations in the ionosphere, $n_e(\mathbf{r}, n)$, scatter radio waves which can be observed by the receiver system of the radar [Dougherty and Farley, 1960]. The emitted radar signal at the transmitter will have a pulse shape $s(n)$ modulated at a central frequency that results in a scattering wave number \mathbf{k} . Using the Born approximation the signal received at time n , $x(n)$, can be represented as the following

$$x(n) = h(n) * \int e^{-j\mathbf{k}\cdot\mathbf{r}} \left(n - \frac{2r}{c} \right) n_e(\mathbf{r}, n) d\mathbf{r}, \quad (2)$$

where $h(n)$ is the receiver filter and the $*$ represents the convolution operator. In modern ISR systems this signal $x(n)$ is then sampled at discrete points in fast-time

127 which will be referred to as n_s . The convolution and sampling operation can be
 128 brought in the integral as the following,

$$x(n_s) = \int e^{-j\mathbf{k}\cdot\mathbf{r}} s\left(n - \frac{2r}{c}\right) n_e(\mathbf{r}, n) h(n_s - n) d\mathbf{r} dn \quad (3)$$

129 Once the signal has been received and sampled the autocorrelation function is
 130 then estimated from the sampled signal $x(n_s)$. The full expression of the underlying
 131 autocorrelation of this signal is the following,

$$\begin{aligned} \langle x(n_s) x^*(n'_s) \rangle &= \int e^{-j\mathbf{k}\cdot(\mathbf{r}'-\mathbf{r})} s\left(n - \frac{2r}{c}\right) s^*\left(n' - \frac{2r'}{c}\right) \\ &\quad h(n_s - n) h(n'_s - n') \langle n_e(\mathbf{r}, n) n_e^*(\mathbf{r}', n') \rangle d\mathbf{r} d\mathbf{r}' dn dn', \quad (4) \end{aligned}$$

132 where r' is the magnitude of the vector \mathbf{r}' . By assuming stationarity of second order
 133 signal statistics along fast time, we can then substitute the the lag variables $\tau \equiv n' - n$,
 134 and $\tau_s \equiv n'_s - n_s$. With these substitutions Equation 4 becomes

$$\begin{aligned} \langle x(n_s) x^*(n_s + \tau_s) \rangle &= \int e^{-j\mathbf{k}\cdot(\mathbf{r}'-\mathbf{r})} s\left(n - \frac{2r}{c}\right) s^*\left(n + \tau - \frac{2r'}{c}\right) \\ &\quad h(n_s - n) h(n_s + \tau_s - n - \tau) \langle n_e(\mathbf{r}, n) n_e^*(\mathbf{r}', n + \tau) \rangle d\mathbf{r} d\mathbf{r}' dn d\tau \quad (5) \end{aligned}$$

135 We can make a simplifying assumption at this point that the space-time autocorre-
 136 lation function of $n_e(\mathbf{r}, t)$, $\langle n_e(\mathbf{r}, n) n_e(\mathbf{r}', n + \tau) \rangle$, will go to zero as the magnitude of
 137 $\mathbf{y} \equiv \mathbf{r}' - \mathbf{r}$ increases beyond the debye length[Farley, 1969]. Thus, the rate which
 138 the spatial autocorrelation goes to zero will be such that $\tau \gg \frac{2\|\mathbf{y}\|}{c}$ allowing us to set
 139 $r = r'$. This allows Equation 5 to be rewritten as

$$\langle x(n_s)x^*(n_s + \tau) \rangle = \int s \left(n - \frac{2r}{c} \right) s^* \left(n + \tau - \frac{2r}{c} \right) h(n_s - n) h^*(n_s + \tau_s - n - \tau) \left[\int e^{-2j\mathbf{k} \cdot \mathbf{y}} \langle n_e(\mathbf{r}, n) n_e^*(\mathbf{y} + \mathbf{r}, n + \tau) \rangle d\mathbf{y} \right] d\mathbf{r} dn d\tau. \quad (6)$$

The inner integral is a spatial Fourier transform evaluated at the wave number of the radar \mathbf{k} . By again asserting stationarity along fast time we can represent the true ACF as the following,

$$R(\tau, \mathbf{r}) = \langle |n_e(\mathbf{k}, r, \tau)|^2 \rangle \equiv \int e^{-2j\mathbf{k} \cdot \mathbf{y}} \langle n_e(\mathbf{r}, b) n_e^*(\mathbf{y} + \mathbf{r}, n + \tau) \rangle d\mathbf{y}. \quad (7)$$

Now Equation 6 becomes

$$\langle x(n_s)x^*(n_s + \tau_s) \rangle = \int \langle |n_e(\tau, \mathbf{k}, \mathbf{r})|^2 \rangle \left[\int s \left(n - \frac{2r}{c} \right) s^* \left(n + \tau - \frac{2r}{c} \right) h(n_s - n) h^*(n_s + \tau_s - n - \tau) dn \right] d\tau dr. \quad (8)$$

If n_s is replaced with $2r_s/c$ we can introduce the range ambiguity function $W(\tau_s, r_s, \tau, r)$ by doing the following substitution,

$$W(\tau_s, r_s, \tau, r) = \int s \left(n - \frac{2r}{c} \right) s^* \left(n + \tau - \frac{2r}{c} \right) h(2r_s/c - n) h^*(2r_s/c + \tau_s - n - \tau) dn. \quad (9)$$

Assuming, for the moment, that $R(\tau, \mathbf{r})$ only varies across the range dimension r we can now represent this in the form of a Fredholm integral equation

$$\langle x(2r_s/c)x^*(2r_s/c + \tau_s) \rangle = \int W(\tau_s, r_s, \tau, r) R(\tau, r) dr d\tau. \quad (10)$$

The range ambiguity function, $W(\tau_s, r_s, \tau, r)$, can be thought of as a smoothing operator along the range and lag dimensions of $R(\tau, r)$.

The spatial ambiguity across the azimuth and elevation angles is determined by the antenna beam pattern. In phased array antennas this beam pattern is ideally the array factor multiplied by the element pattern [Balanis, 2005]. The array factor is determined by a number of things including the element spacing and the wave number of the radar, k . For example, by making idealized assumptions with no mutual coupling and that the array elements are cross dipole elements, AMISR systems will have the following antenna pattern for pointing angle (θ_s, ϕ_s) ,

$$F(\theta_s, \phi_s, \theta, \phi) = \frac{1}{2}(1 + \cos(\theta)^2) \left[\frac{1}{MN} (1 + e^{j(\psi_y/2 + \psi_x)}) \frac{\sin((M/2)\psi_x)}{\sin(\psi_x)} \frac{\sin((N/2)\psi_x)}{\sin(\psi_x/2)} \right]^2, \quad (11)$$

where $\psi_x = -kd_x(\sin \theta \cos \phi - \sin \theta_s \cos \phi_s)$, $\psi_y = -kd_y(\sin \theta \sin \phi - \sin \theta_s \sin \phi_s)$ and M is the number of elements in the x direction of the array, and N is the number of elements in the y direction(see Appendix: A for derivation).

The spatial ambiguity is a separable function made up of the components of $W(\tau_s, \tau, r_s, r)$ and $F(\theta_s, \phi_s, \theta, \phi)$. These two functions can be combined by multiplying the two, creating the spatial ambiguity function $K(\tau_s, \mathbf{r}_s, \tau, \mathbf{r})$, and then doing a volume integration. This yields an estimate of the ACF using only one pulse, which will be referred to as $\rho(\tau_s, \mathbf{r}_s)$,

$$\rho(\tau_s, \mathbf{r}_s) = \int F(\theta_s, \phi_s, \theta, \phi) W(\tau_s, r_s, \tau, r) R(\tau, \mathbf{r}) dV, \quad (12)$$

$$= \int K(\tau_s, \mathbf{r}_s, \tau, \mathbf{r}) R(\tau, \mathbf{r}) dV. \quad (13)$$

A rendering of an example of this full spatial ambiguity function for an uncoded long pulse and antenna pattern in Equation 11 for four beams can be seen in Figure 3.

This one pulse ACF estimate represents a single sample of a random process. In order to create a usable estimate, multiple samples of this ACF need to be averaged together to reduce the variance to sufficient levels in order to fit the estimate to a theoretical ACF that is tied to plasma parameter values. To show the impact of this averaging to create the estimate of the ACF we will add slow-time dependence to $R(\tau, \mathbf{r}, t)$ along with another separable function $G(t_s, t)$ to the kernel. This function $G(t_s, t)$, can be thought of as a sampling and blurring kernel for the ACF if the plasma parameters change with in an NCPI. Since the amount of time that the radar pulse is illuminating the plasma in a point of space is very short compared to IPP, $G(t_s, t)$ can take the form of a summation of Dirac delta functions

$$G(t_s, t) = \sum_{j=0}^{J-1} \alpha_j \delta(t - t_s - jT_{PRI}), \quad (14)$$

where J is the number of pulses used over a NCPI, T_{PRI} is the PRI time period and α_j is the weights that the radar assigns to the pulses. The weights are generally set to $1/J$ to simply average the pulses. With Equation 14 incorporated into the overall ambiguity we see the full integral equation,

$$\rho(\tau_s, \mathbf{r}_s, t_s) = \int L(\tau_s, \mathbf{r}_s, t_s, \tau, \mathbf{r}, t) R(\tau, \mathbf{r}, t) dV dt. \quad (15)$$

The final kernel, $L(\tau_s, \mathbf{r}_s, t_s, \tau, \mathbf{r}, t) = G(t_s, t)K(\tau_s, \mathbf{r}_s, \tau, \mathbf{r})$, encompasses the full space-time ambiguity.

2.3. Ambiguity after Frame Transformation

We will now focus on the impact of the motion of plasma as it is going through the field of view of the radar. We will assume that the radar is integrating over a length of time T beginning at t_s . The kernel L will be represented as a separable function K and G as in Equation 15. In this case G will be a summation of Dirac delta functions with weights of $1/J$. This will change Equation 15 to the following,

$$\rho(\tau_s, \mathbf{r}_s, t_s) = \int K(\tau_s, \mathbf{r}_s, \tau, \mathbf{r}) \left[(1/J) \int_{t_s}^{t_s+T} \sum_{j=0}^{J-1} \delta(t - t_s - jT_{PRI}) R(\tau, \mathbf{r}, t) dt \right] dV. \quad (16)$$

Of specific interest are instances in the high latitude ionosphere where embedded plasma structures are moving due to the electric field of the magnetosphere. Because of this it will be assumed that the plasma is a rigid object and will not deform with respect to \mathbf{r} over time period $[t_0, t_0 + T]$ where $T = JT_{PRI}$ is the time for one NCPI. Also it will be assumed that it will be moving with a constant velocity \mathbf{v} . Thus $R(\tau, \mathbf{r}, t) \Rightarrow R(\tau, \mathbf{r} + \mathbf{v}t)$. The assumption of rigidity is possible to make over the time period of the NCPI, on the order of a few minutes, while the plasma moves through the field of view of the radar. One example can be taken from the high latitude ionosphere while large scale features in structures such as patches decay on the order of hours [Tsunoda, 1988]. This assumption is useful because it shows the utility of this frame work to analyze the impacts on the true resolution of the ISR systems. With these assumptions Equation 16 becomes,

$$\rho(\tau_s, \mathbf{r}_s, t_s) = (1/J) \int \int_{t_s}^{t_s+T} \sum_{j=0}^{J-1} \delta(t - t_s - jT_{PRI}) K(\tau_s, \mathbf{r}_s, \tau, \mathbf{r}) R(\tau, \mathbf{r} + \mathbf{v}t) dt dV \quad (17)$$

A change of variables to $\mathbf{r}' = \mathbf{r} + \mathbf{v}t$ acts as a Galilean transform and applies a warping to the kernel, changing the frame of reference. Since $R(\tau, \mathbf{r}')$ is no longer dependent on t Equation 17 becomes,

$$\rho(\tau_s, \mathbf{r}_s, t_s) = (1/J) \int \left[\sum_{j=0}^{J-1} K(\tau_s, \mathbf{r}_s, \tau, \mathbf{r}' - \mathbf{v}(t_s + jT_{PRI})) \right] R(\tau, \mathbf{r}') dV. \quad (18)$$

By performing the integration in t the problem can now be simplified further back to a Fredholm integral equation by simply replacing the terms in the square brackets as a new kernel $A(\tau_s, \mathbf{r}_s, t_s, \tau, \mathbf{r}')$,

$$\rho(\tau_s, \mathbf{r}_s, t_s) = \int A(\tau_s, \mathbf{r}_s, t_s, \tau, \mathbf{r}') R(\tau, \mathbf{r}') dV. \quad (19)$$

The impact of the plasma velocity on the ambiguity function can be seen in Figure 4. This is the same ambiguity as seen in Figure 3 but with a velocity of 500 m/s in the y direction over a period of 2 minutes. This velocity creates a larger ambiguity function in the frame of reference of the moving plasma.

The operator A can be determined through knowledge of the radar system's beam pattern along with the experiment's pulse pattern, integration time and velocity of the plasma. This velocity \mathbf{v} can be estimated by taking measurements of the Doppler shift and using a methodology seen in *Butler et al.* [2010]. Once the operator has

been determined standard processing techniques can be used as if the plasma is not moving, under the previous assumptions.

3. Simulation

Although Figures 3 and 4 show the spatial extent of the space-time ambiguity function both with and without target motion, the impact of this on the reconstruction data can better shown through simulation. To do so we show data from a 3-D ISR simulator with a known ionosphere. In the following section we describe this simulator along with two case studies to show the impact of this ambiguity on properly reconstructing the parameters in the ionosphere.

3.1. Simulator

The simulator creates data by deriving time filters from the autocorrelation function and applying them to complex white Gaussian noise generators. Stating this in another way, every point in time and space has a noise plant and filter structure as in Figure 5. The data is then scaled and summed together according to its location in range and angle space to radar. For this simulation the data points are only used if they are within 1.1° of the center beam which is a simplification of the AMISR beam pattern.

After the IQ data has been created it is processed to create estimates of the ACF at desired points of space. This processing a follows flow chart seen in Figure 6.

The sampled I/Q can be represented as $x(n_s) \in \mathbb{C}^N$ where N is the number of samples in an inter pulse period. At this point the first step in estimating the auto-

correlation function is taken. For each range gate $m \in 0, 1, \dots, M-1$ an autocorrelation is estimated for each lag of $l \in 0, 1, \dots, L-1$. This operation of forming the ACF estimates repeats for each pulse, $j \in 0, 1, \dots, J-1$, and is then summed over the J pulses. The entire operation to form the initial estimate of $\hat{R}(m, l)$ is the following,

$$\hat{R}(m, l) = \sum_{j=0}^{J-1} x(m - \lfloor l/2 \rfloor, j) x^*(m + \lceil l/2 \rceil, j). \quad (20)$$

The case shown in Equation 20 is a centered lag product, which is what we used for our simulations, but other types of lag product calculations are possible as well. In the centered lag product case, range gate index m and sample index n can be related by $m = n_s - \lfloor L/2 \rfloor$ and the maximum lag and sample relation is $M = N - \lfloor L/2 \rfloor$.

After the lag products have been formed an estimate of the noise correlation is subtracted out of $\hat{R}(m, l)$, which is defined as $\hat{R}_w(m, l)$,

$$\hat{R}_w(m_w, l) = \sum_{j=0}^{J-1} w(m_w - \lfloor l/2 \rfloor, j) w^*(m_w + \lceil l/2 \rceil, j), \quad (21)$$

where $w(n_w)$ is the background noise process of the radar.

The final estimate of the autocorrelation function after the noise subtraction and summation rule will be represented by $\hat{R}_f(m, l)$. At this point a summation rule is applied and the data is sent off to be fit. The final parameters are derived through a standard Levenberg-Marquart non-linear least-squares fitting of n_e, T_i, T_e [Levenberg, 1944].

3.2. Case 1

The first example is a simple case of a small plasma enhancement moving through the radar field of view. This case is meant to model conditions expected in the polar cap ionosphere under southward IMF conditions [Dahlgren *et al.*, 2012b]. The background electron density varies in altitude as a Chapman function, shown in Figure 7, while the electron and ion temperature remains constant.

Embedded in the background there is a 35 km radius sphere of enhanced electron density of $5 \times 10^{10} \text{ m}^{-3}$ centered at 400 km altitude moving at 500 m/s along the \mathbf{y} direction. Images from this phantom can be seen in Figure 8. To simplify the simulation the atmosphere is assumed to be 100% Oxygen ions. For the ease of comparison the phantom is only shown in areas where it is in the radar's field of view. The positions of the 121 beam used for this case can be seen in Figure 9.

Because only the electron density is varying the fitting method becomes simply a power estimate as the electron density is directly proportional to the return power if the temperature ratio is known. This example allows the blurring from the space-time ambiguity function can be observed easier, while also showing trade offs between statistical variance and blurring.

Using the phantom we can see how just simply changing the integration time can impact the reconstruction. In Figure 10 we can see a case where only 10 pulses are used for the reconstruction, which corresponds to an integration time of about 9 seconds. The enhancement can be seen as it moves through the field of view although there is that there is a high amount of variance in the reconstruction. Figure 11 shows the reconstruction with 200 pulses, 3 minute integration time. The variability has

been reduced but there is a large amount of blurring of the enhancement as it moves through the field of view.

In order to give a comparison based on integration time a phantom was also created one with no motion. This can be seen in the first pane Figure 12. An image using the same integration time as in Figure 10 for the stationary phantom is the center pane in Figure 12. Another image using the longer integration time can be seen in right pane of Figure 12. These images show that the blurring is on the same order between both integration times.

3.3. Case 2

Secondly, we show results of a simulation of the plasma density enhancement through the field of view but the ion and electron temperatures are allowed to vary. This case will represent a departure from the standard blurring problem seen in image processing because the parameters to be estimated are related to the data through a non-linear expression. The resulting ACF estimates though are created through a linear blurring kernel in both time and space.

We again use a plasma enhancement moving through the field of view at 500 m/s but the electron and ion temperature varies with time and altitude. The the background ion and electron temperature vs. height can be seen in Figure 14. As the electron density enhancement travels through the field of view the temperatures drop by the same ratio that the electron density is enhanced. This is done to keep the variance the same at each point in space for a given number of pulses integrated..

The phantoms for each parameter at approximately 402 seconds can be seen in Figure 14. The reconstruction of this field at the same time can be seen in Figure 15. The reconstruction does not seem to show the electron density enhancement even in a blurred form.

In order to determine the reason behind the poor reconstruction we look at the fit surface of one of the points in the reconstruction. The fit surface is the error between the estimated ISR spectrum and the spectrum derived from the different parameters. Comparing the points $\mathbf{r} = [10, 10, 400]\text{km}$ and the closest reconstruction point in the radar field of view, $\mathbf{r}_s = [6.72, 1.80, 398.77]$. The time was chosen so the integrated measurement would be centered over the time when the enhancement moved through this point. During this time period the radar will integrate over two distributions of plasma at this point. The plasma at point \mathbf{r} are $N_e = 1.96 \times 10^{10}\text{m}^{-3}$, $T_i = 1064$ °K and $T_e = 1324$ °K when there is no enhancement traveling through. When the enhancement is traveling through this point $N_e = 5 \times 10^{10}\text{m}^{-3}$, $T_i = 416$ °K and $T_e = 518$ °K. The speed of the enhancement, which is going at 500 m/s, causes about two-thirds of the pulses to correspond to the enhanced plasma during the integration.

The fit results in the parameter values at \mathbf{r} are $N_e = 2.36 \times 10^{10}\text{m}^{-3}$, $T_i = 973$ °K and $T_e = 500$ °K. The fit surface was formed over the parameter space of N_e 1×10^{10} to $1 \times 10^{11}\text{m}^{-3}$, and for both T_e and T_i were over an values 100 to 1500 °K. In this case the fit surface showed that the global minimum was located in the same found in the same location as found by the Levenberg-Marquart algorithm. A two dimensional cut of the fit surface at $N_e = 2.43 \times 10^{10}$ and showing its variability between T_i and

T_e in Figure 16. Since this is a global minimum supports the possibility of the non uniformity of the plasma parameters causing an erroneous fit. Mixtures of different plasma populations causing erroneous fits have been shown before such as in *Knudsen et al.* [1993].

The spectrums that are yielded from the parameters along with what was estimated can be seen in Figure 17. In this case it can be seen that the spectrum estimated from the data has been reduced by the averaging over time and space which has lowered its power dramatically thus making it more similar to a spectrum with the improper values.

4. Possible Mitigation Techniques

As can be seen from the previous sections a number of different types of errors can occur due to this type of space-time ambiguity function. There are a number of possible approaches one could take in order to produce an improved data product from electronically scanned ISR measurements. This discussion isn't meant to be exhaustive but instead, to give an idea of the utility of this framework. In order to focus this section we will concentrate on methods to remove motion blur type errors that occur when plasma is moving through the field of view, and techniques to improve the spatio-temporal resolution of the measurements.

In order to reduce the impact from plasma parcel motion, a relatively simple approach would involve processing the data in the frame of reference of the moving density field. The convection velocity is manifested as a bulk Doppler shift in the

ISR spectrum. Under the assumptions applied in our examples, this Doppler shift is independent of the other parameters, and so \mathbf{v} in Equation 18 could be extracted using the analysis described by *Heinselman and Nicolls* [2008] and *Butler et al.* [2010]. After measuring the velocity instead of integrating in the same beam one could integrate across different beams using this knowledge. This would allow for ACF to be formed from the same populations of plasma as it moves through the field of view.

If one wants to improve the resolution of the the plasma parameters it may be necessary to do some sort of regularization. There are two type of regularization that can be applied in this case the first is parameter based regularization, like full profile analysis *Holt et al.* [1992]; *Hysell et al.* [2008]. We will use the term parameter based regularization in this case means applying constraints to the physical parameters that are often determined after fitting. Currently full profile analysis has only been applied along the range dimension and not in all three spatial dimensions. Still if full profile analysis is to be extended so it can be used in ESA systems a forward model between the actual ACF and the one measured in the radar would be needed. This is encompassed within Equation 15.

The other method we will refer to as data based regularization. This term infers the application of constraints to the estimates of the autocorrelation functions and then fitting. The constraints usually deal with how the data changes over time and space by constraining the energy of the ACFs [*Virtanen et al.*, 2008; *Nikoukar et al.*, 2008] or its derivative [*Nikoukar*, 2010]. A simplification of the data based regularization is that one is doing a deconvolution operation on the ACFs. This has

an advantage that one can use linear inverse theory estimate the lags and then do the fit. Unlike with parameter based regularization schemes such as full profile analysis where ionospheric parameters are directly estimated and regularized. Because of this data based regularization has the advantage of generally being more computationally tractable than parameter based. One of the drawbacks though with data based regularization though is that is very difficult to argue what constraint would be "correct" to use. While in full profile analysis the constraints are based on known physics in the ionosphere to create a measurement. In any case in order to extend the methodology from *Virtanen et al.* [2008] and *Nikoukar et al.* [2008] one can use the kernel L if trying to improve the measurements from an ESA ISR.

5. Conclusion

This publication has laid the foundation for the optimal analysis of volumetric data acquired from electronically steerable ISR systems. This framework allows for taking into account the antenna beam pattern, pulse pattern and time integration. Through simulation we have shown how plasma motion can impact reconstruction of parameters which compounded with the non-linear nature of the parameter fitting step can create errors which are hard to predict. Lastly we briefly outlined a number of possible approaches improving measurements derived from ESA ISRs.

Appendix A: Derivation of Idealized AMISR Array Pattern

The current antenna on the AMISR systems is made up 8x16 set of panel of half wave cross dipoles. Each panel has 32 cross dipoles in a 8x4 hexagonal configuration.

In the current set up at the Poker Flat site this yields at 4096 element array in a 64x64 element hexagonal configuration.

In order to simplify the antenna can be treated as two rectangular arrays of cross dipoles interleaved together. In the x direction each of these arrays will have a spacing of $2d_x$ with $M/2$ elements. The y direction will be of length N elements and spacing d_y . Using basic planar phase array theory, [Balanis, 2005], we can start with the linear array pattern from the first array can be represented as

$$E_1(\theta, \phi) = \sum_{m=1}^{M/2} \sum_{n=1}^N e^{-j2(m-1)kd_x \sin \theta \cos \phi - j(n-1)kd_y \sin \theta \sin \phi}. \quad (\text{A1})$$

Since the second array can be thought of a shifted version of the first in the x direction we get the following

$$E_2(\theta, \phi) = \sum_{m=1}^{M/2} \sum_{n=1}^N e^{-j(2m-1)kd_x \sin \theta \cos \phi - j(n-1/2)kd_y \sin \theta \sin \phi}. \quad (\text{A2})$$

In order to simplify notation we will make the following substitutions, $\psi_x = -kd_x \sin \theta \cos \phi$, $\psi_y = -kd_y \sin \theta \sin \phi$. Using Equations A1 and A2 we can see the following relationship,

$$E_2(\theta, \phi) = e^{j(\psi_y/2 + \psi_x)} E_1(\theta, \phi) = \sum_{m=1}^{M/2} \sum_{n=1}^N e^{-j2(m-1)\psi_x - j(n-1)\psi_y}. \quad (\text{A3})$$

Adding E_1 and E_2 together we get the following linear array pattern

$$\begin{aligned}
E(\theta, \phi) &= (1 + e^{j(\psi_y/2 + \psi_x)}) \sum_{m=1}^{M/2} \sum_{n=1}^N e^{-j2(m-1)\psi_x - j(n-1)\psi_y}. \\
&= \frac{1}{MN} (1 + e^{j(\psi_y/2 + \psi_x)}) \frac{\sin((M/2)\psi_x)}{\sin(\psi_x)} \frac{\sin((N/2)\psi_y)}{\sin(\psi_y/2)}.
\end{aligned} \tag{A4}$$

Since the array is steerable this can be taken into account in the equations by simply changing the definitions of ψ_x and ψ_y to $\psi_x = kd_x(\sin \theta \cos \phi - \sin \theta_s \cos \phi_s)$, and $\psi_y = kd_y(\sin \theta \sin \phi - \sin \theta_s \sin \phi_s)$. Lastly the antenna pattern of a single cross dipole can be represented as $\frac{1}{2}(1 + \cos^2(\theta))$ [Balanis, 2005]. By taking the squared magnitude of the array factor and multiplying it with the pattern of the dipole we get Equation 11,

$$F(\theta_s, \phi_s, \theta, \phi) = \frac{1}{2}(1 + \cos^2(\theta))^2 \left| \frac{1}{MN} (1 + e^{j(\psi_y/2 + \psi_x)}) \frac{\sin((M/2)\psi_x)}{\sin(\psi_x)} \frac{\sin((N/2)\psi_y)}{\sin(\psi_y/2)} \right|^2. \tag{A5}$$

References

- (2005), Eiscat 3d design specification document.
- (2014), Amisr overview.
- Balanis, C. A. (2005), *Antenna Theory: Analysis and Design*, Wiley-Interscience.
- Butler, T. W., J. Semeter, C. J. Heinselman, and M. J. Nicolls (2010), Imaging of region drifts using monostatic phased-array incoherent scatter radar, *Radio Sci.*, 45(5), RS5013, doi:10.1029/2010RS004364.
- Dahlgren, H., J. L. Semeter, K. Hosokawa, M. J. Nicolls, T. W. Butler, M. G. Johnsen, K. Shiokawa, and C. Heinselman (2012a), Direct three-dimensional imaging of polar

ionospheric structures with the resolute bay incoherent scatter radar, *Geophysical Research Letters*, 39(5), n/a–n/a, doi:10.1029/2012GL050895.

Dahlgren, H., G. W. Perry, J. L. Semeter, J. P. St. Maurice, K. Hosokawa, M. J. Nicolls, M. Greffen, K. Shiokawa, and C. Heinselman (2012b), Space-time variability of polar cap patches: Direct evidence for internal plasma structuring, *Journal of Geophysical Research: Space Physics*, 117(A9), A09,312, doi:10.1029/2012JA017961.

Dougherty, J. P., and D. T. Farley (1960), A theory of incoherent scattering of radio waves by a plasma, *Proceedings of the Royal Society of London. Series A, Mathematical and Physical Sciences*, 259(1296), pp. 79–99.

Dougherty, J. P., and D. T. Farley (1963), A theory of incoherent scattering of radio waves by a plasma, 3 scattering in a partly ionized gas, *Journal of Geophysical Research*, 68, 5473.

Farley, D. T. (1969), Incoherent scatter correlation function measurements, *Radio Sci.*, 4(10), 935–953.

Farley, D. T., J. P. Dougherty, and D. W. Barron (1961), A theory of incoherent scattering of radio waves by a plasma ii. scattering in a magnetic field, *Proceedings of the Royal Society of London. Series A, Mathematical and Physical Sciences*, 263(1313), pp. 238–258.

Hagfors, T. (1961), Density fluctuations in a plasma in a magnetic field, with applications to the ionosphere, *Journal of Geophysical Research*, 66(6), 1699–1712, doi:10.1029/JZ066i006p01699.

- Heinselman, C. J., and M. J. Nicolls (2008), A bayesian approach to electric field and e-region neutral wind estimation with the poker flat advanced modular incoherent scatter radar, *Radio Science*, *43*(5), n/a–n/a, doi:10.1029/2007RS003805.
- Holt, J. M., D. A. Rhoda, D. Tetenbaum, and A. P. van Eyken (1992), Optimal analysis of incoherent scatter radar data, *Radio Science*, *27*(3), 435–447, doi:10.1029/91RS02922.
- Hysell, D. L., F. S. Rodrigues, J. L. Chau, and J. D. Huba (2008), Full profile incoherent scatter analysis at jicamarca, *Annales Geophysicae*, *26*(1), 59–75, doi:10.5194/angeo-26-59-2008.
- Knudsen, D. J., G. Haerendel, S. Buchert, M. C. Kelley, Å. Steen, and U. Brändström (1993), Incoherent scatter radar spectrum distortions from intense auroral turbulence, *Journal of Geophysical Research: Space Physics*, *98*(A6), 9459–9471, doi:10.1029/93JA00179.
- Lehtinen, M. S., and A. Huuskonen (1996), General incoherent scatter analysis and {GUISDAP}, *Journal of Atmospheric and Terrestrial Physics*, *58*(1–4), 435 – 452, doi:http://dx.doi.org/10.1016/0021-9169(95)00047-X, Selected papers from the sixth international Eiscat Workshop.
- Levenberg, K. (1944), A method for the solution of certain non-linear problems in least squares, *Quarterly of Applied Mathematics*, *2*, 164–168.
- Nicolls, M. J., and C. J. Heinselman (2007), Three-dimensional measurements of traveling ionospheric disturbances with the Poker Flat Incoherent Scatter Radar, *Geophysical Research Letters*.

- 433 Nikoukar, R. (2010), Near-optimal inversion of incoherent scatter radar
434 measurements- coding schemes, processing techniques, and experiments, Ph.D. the-
435 sis, University of Illinois at Urbana-Champaign.
- 436 Nikoukar, R., F. Kamalabadi, E. Kudeki, and M. Sulzer (2008), An efficient near-
437 optimal approach to incoherent scatter radar parameter estimation, *Radio Science*,
438 *43*(5), n/a–n/a, doi:10.1029/2007RS003724.
- 439 Richards, M. A. (2005), *Fundamentals of Radar Signal Processing*, McGraw-Hill.
- 440 Semeter, J., T. Butler, C. Heinselman, M. Nicolls, J. Kelly, and D. Hamp-
441 ton (2009), Volumetric imaging of the auroral ionosphere: Initial results from
442 pfisr, *Journal of Atmospheric and Solar-Terrestrial Physics*, *71*, 738 – 743, doi:
443 10.1016/j.jastp.2008.08.014, jce:titleAdvances in high latitude upper atmospheric
444 science with the Poker Flat Incoherent Scatter Radar (PFISR)i/ce:titlej.
- 445 Tsunoda, R. T. (1988), High-latitude F region irregularities: A review and synthesis,
446 *Reviews of Geophysics*.
- 447 Virtanen, I. I., M. S. Lehtinen, and T. Nygrén (2008), Lag profile inversion method
448 for EISCAT data analysis, *Annales . . .*
- 449 Zettergren, M., J. Semeter, P.-L. Blelly, G. Sivjee, I. Azeem, S. Mende, H. Gleisner,
450 M. Diaz, and O. Witasse (2008), Optical estimation of auroral ion upflow: 2. a
451 case study, *Journal of Geophysical Research: Space Physics*, *113*(A7), n/a–n/a,
452 doi:10.1029/2008JA013135.

453 **Acknowledgments.** (Text here)

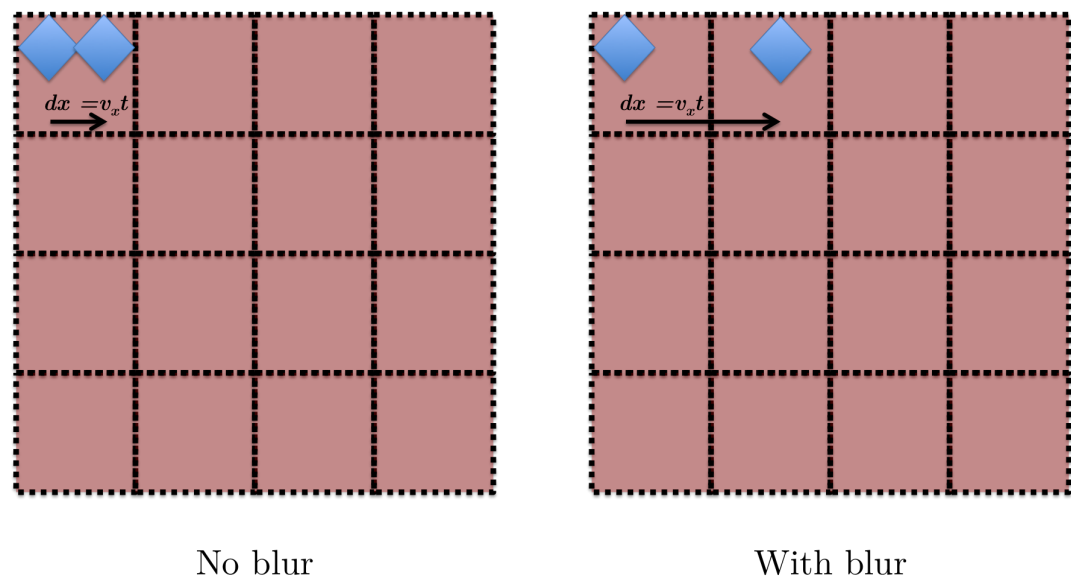


Figure 1. CCD resolution cell diagram both with and without blurring

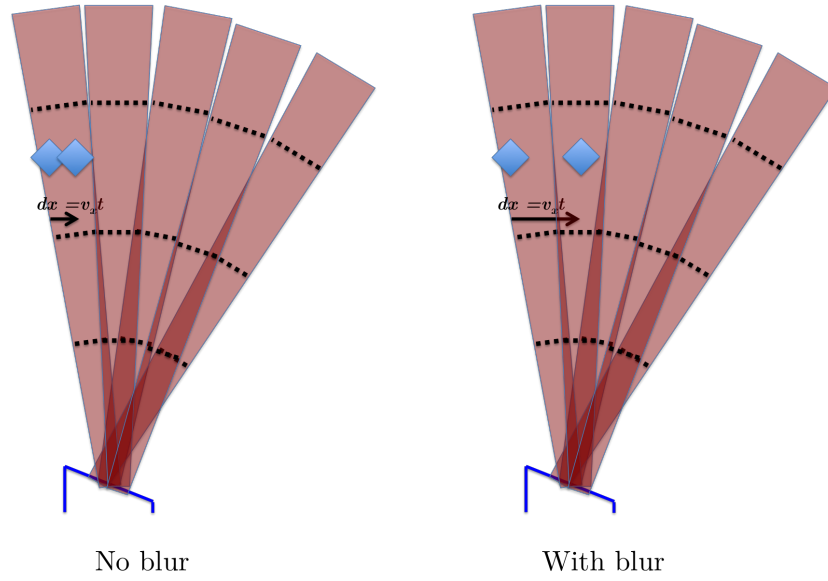


Figure 2. ISR resolution cell diagram both with and without blurring

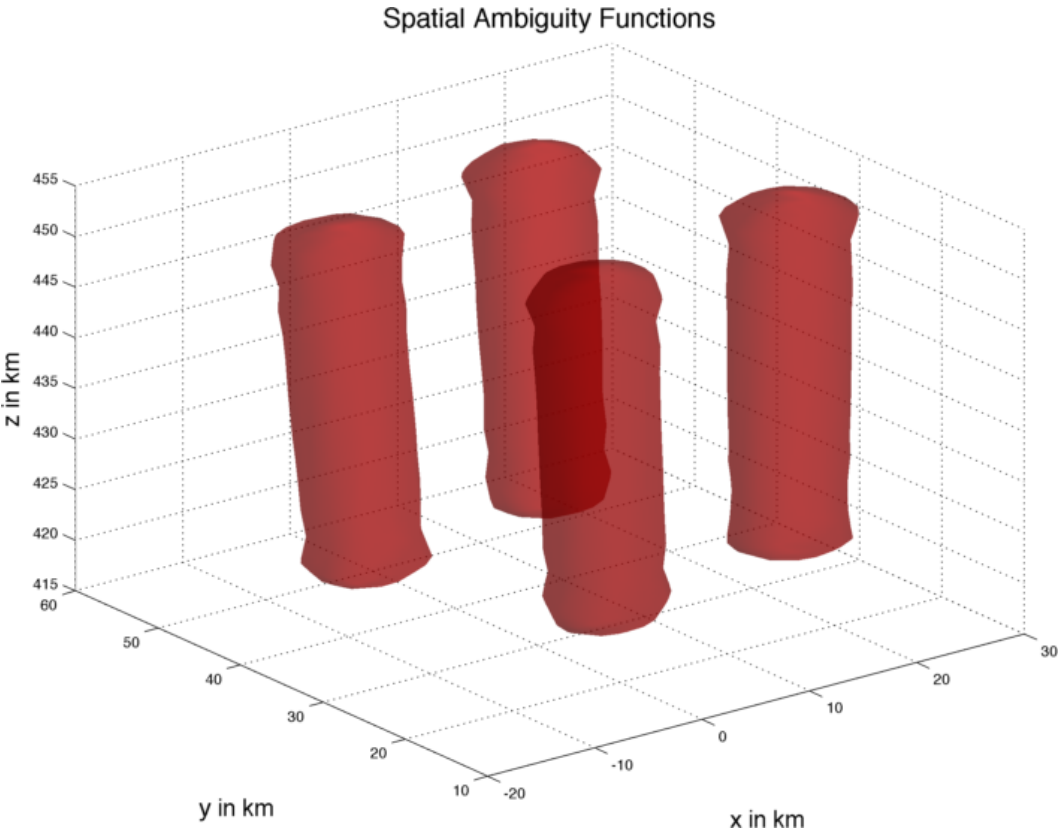


Figure 3. Full spatial ambiguity function

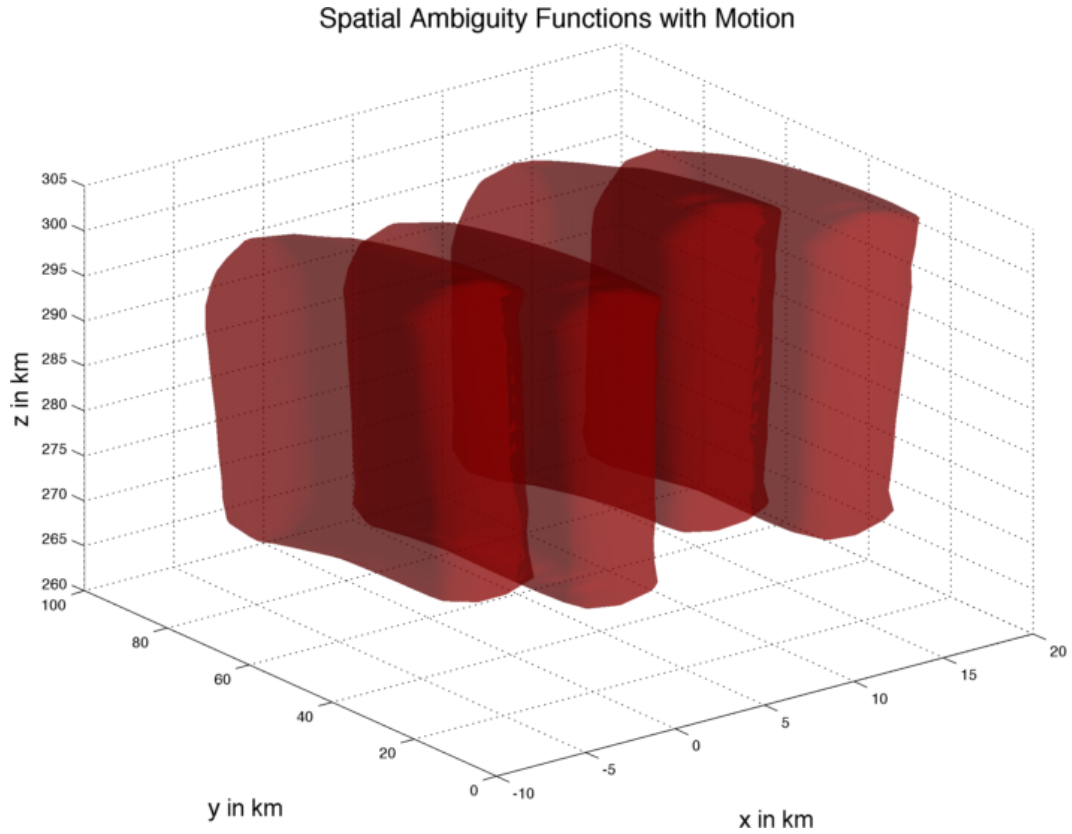


Figure 4. Full spatial ambiguity function with target motion

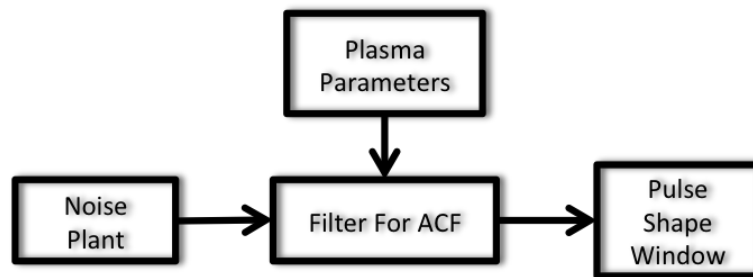


Figure 5. I/Q simulator diagram

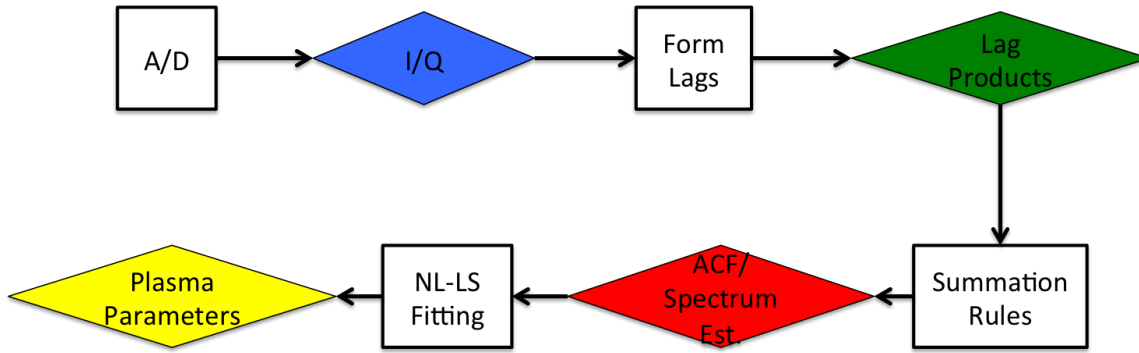


Figure 6. ISR processing chain.

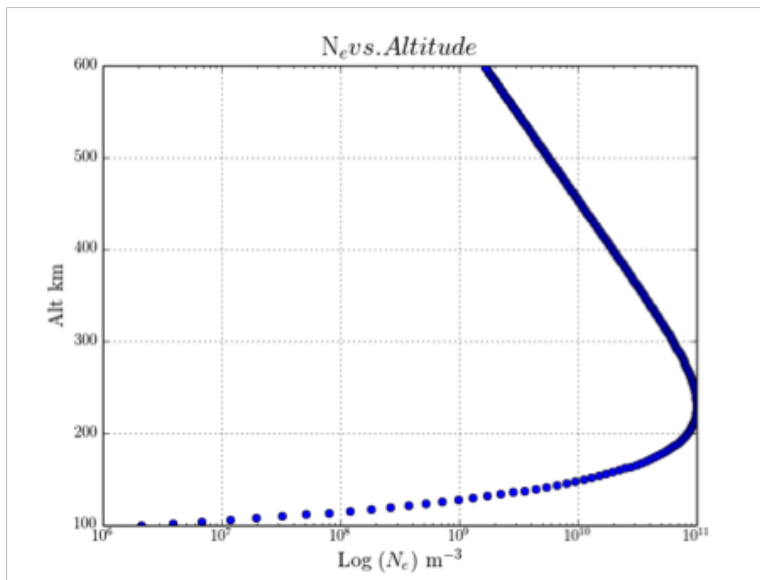


Figure 7. Simulated electron density verses altitude.

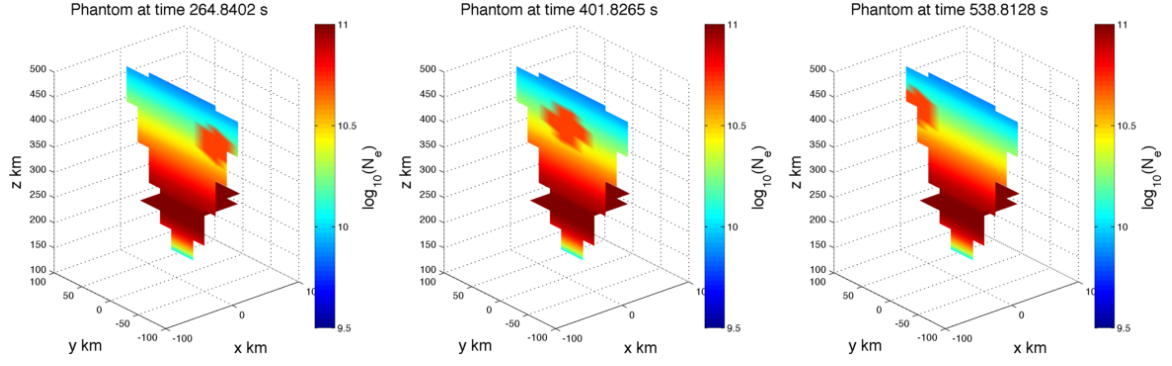


Figure 8. Images of input N_e for the simulation at three different times.

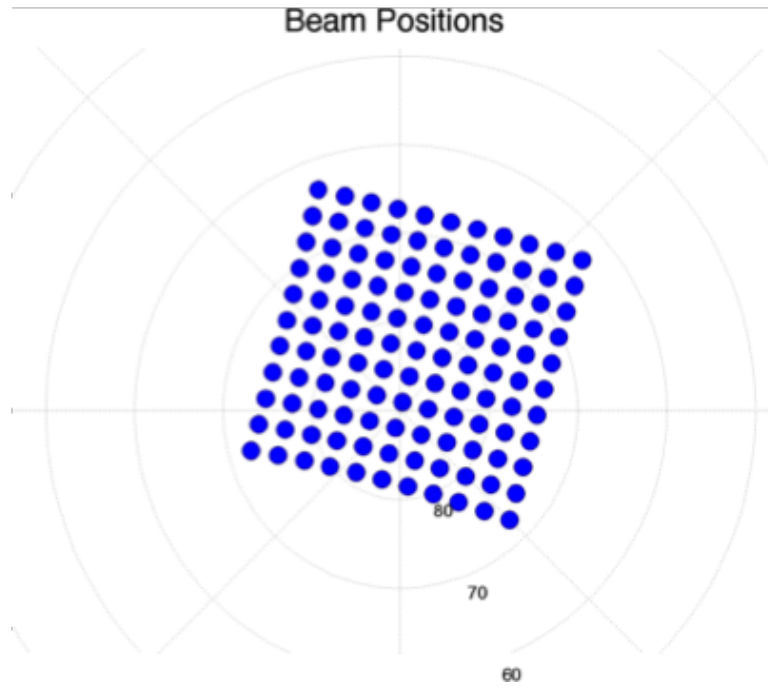


Figure 9. Radar beam pattern used in the simulations

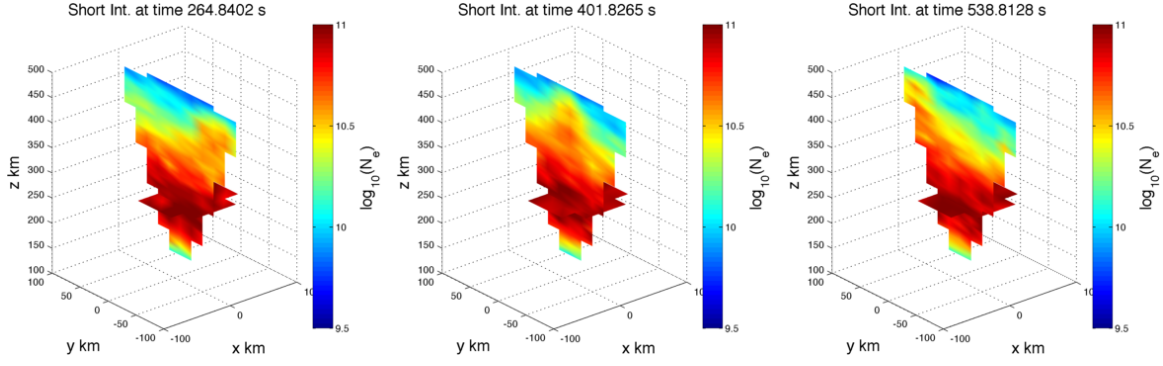


Figure 10. Reconstructions of N_e using 10 Pulses at three different times.

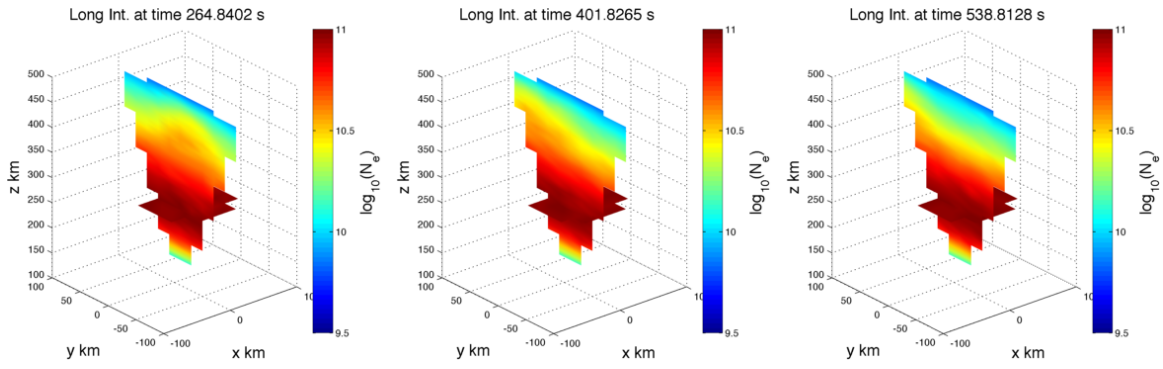


Figure 11. Reconstructions of N_e using 200 Pulses at three different times.

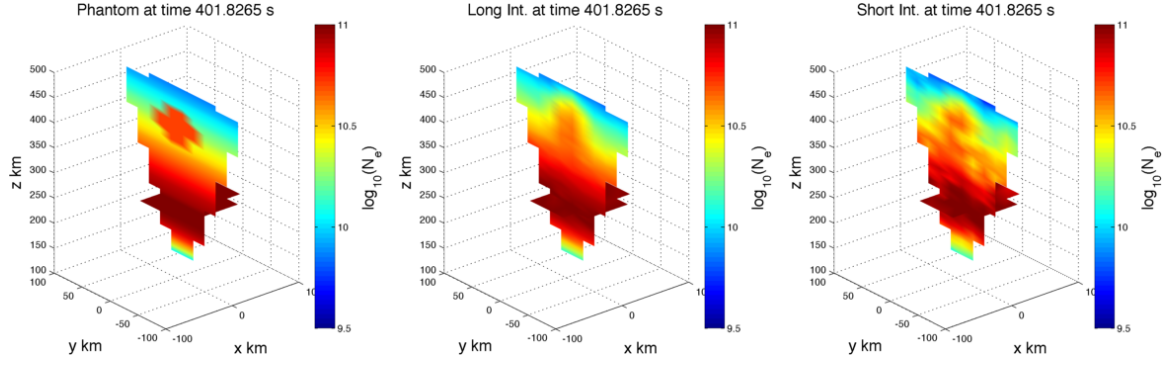


Figure 12. Stationary phantom of N_e along with reconstructions using 10 and 200 pulses.

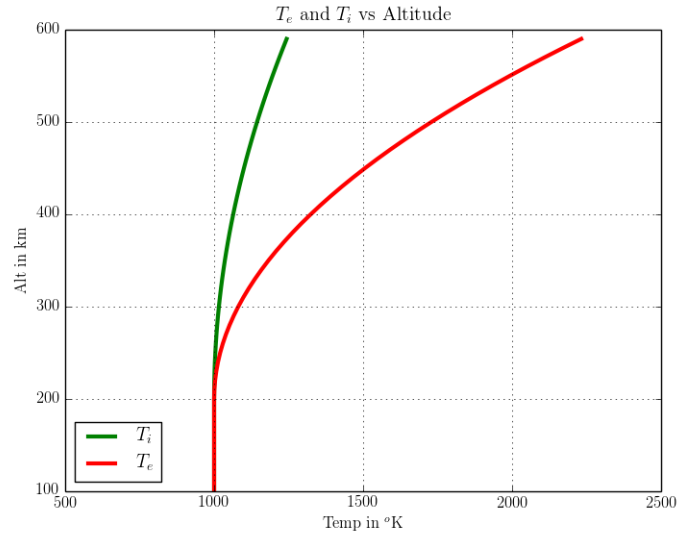


Figure 13. Ion & electron temperature verses height for simulation.

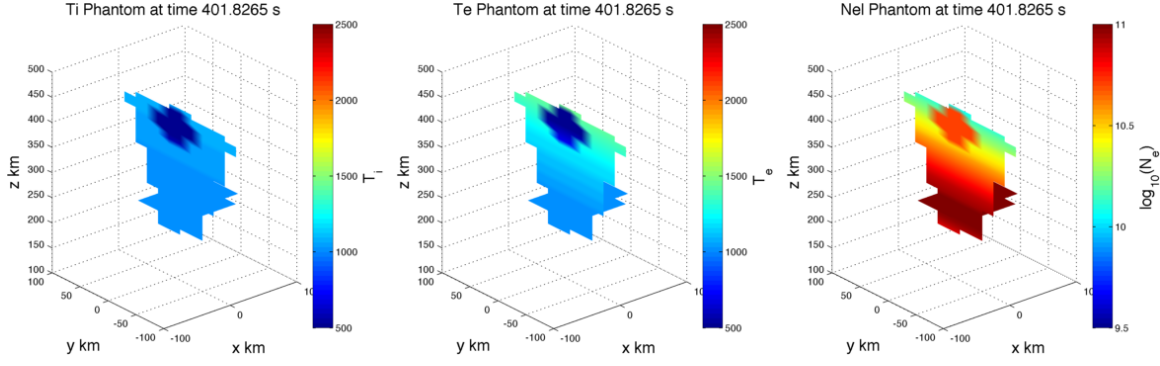


Figure 14. Phantoms of T_i , T_e and N_e at $t = 401.8265$ s.

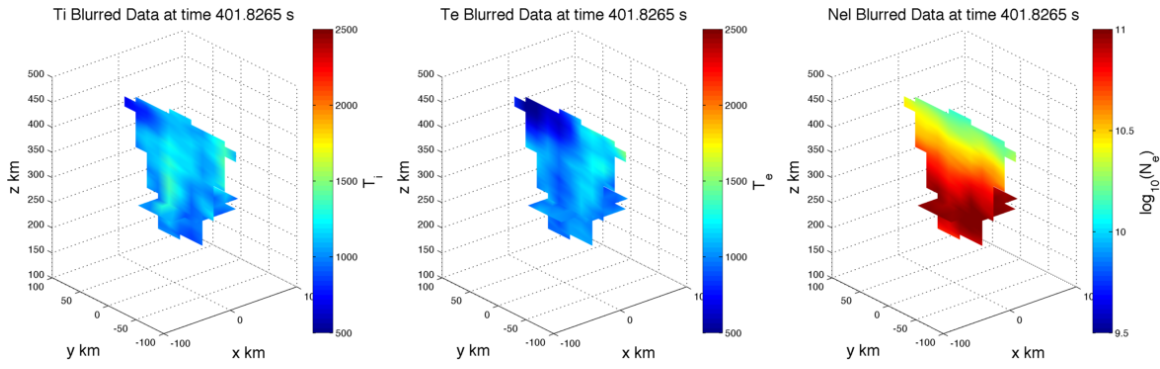


Figure 15. Interpolated reconstructions of T_i , T_e and N_e at $t = 401.8265$ s.

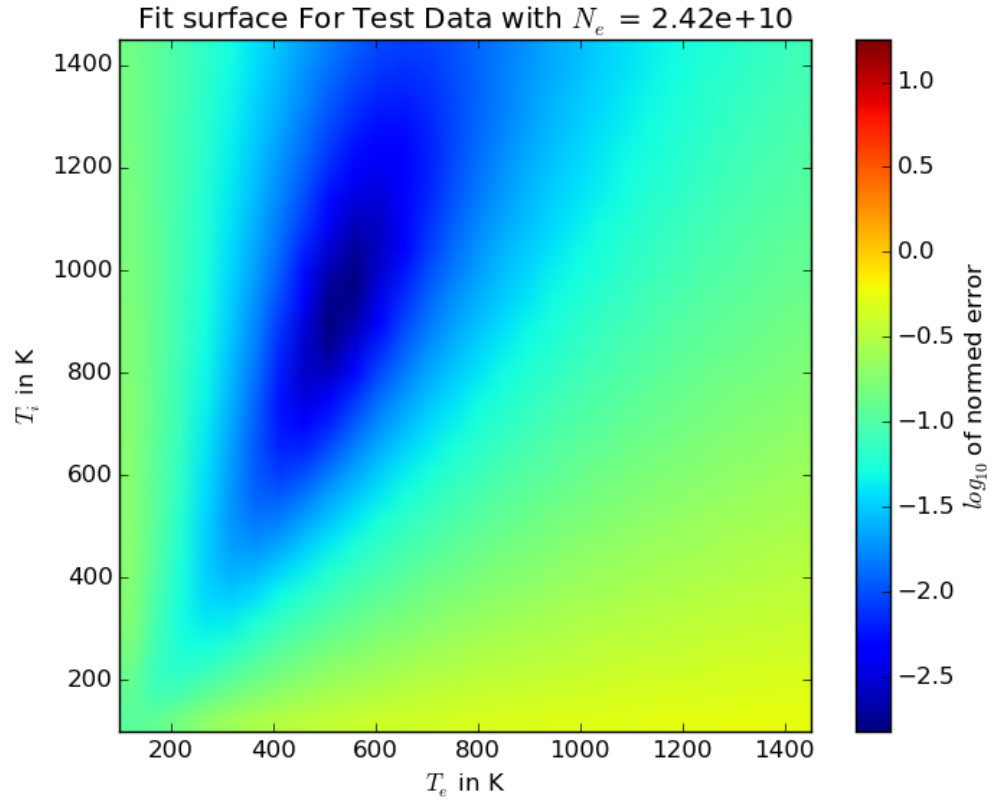


Figure 16. Fit surface spectrum at $\mathbf{r}_s = [6.72, 1.80, 398.77]$.

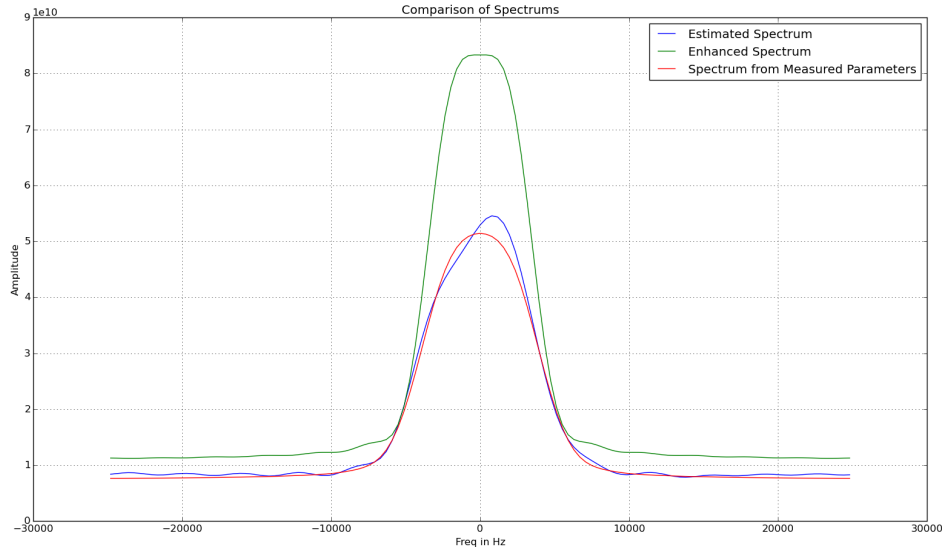


Figure 17. Estimated spectrum from from $\mathbf{r}_s = [6.72, 1.80, 398.77]$ along with spectrum from measured parameters and from enhanced plasma.